Measurement of the $p\bar{p} \to t\bar{t} + X$ production cross section at $\sqrt{s} = 1.96$ TeV in the fully hadronic decay channel

V. M. Abazov,[35] B. Abbott,[75] M. Abolins,[65] B. S. Acharya,[28] M. Adams,[51] T. Adams,[49] E. Aguilo,[5] S. H. Ahn,[30] M. Ahsan,[59] G. D. Alexeev,[35] G. Alkhazov,[39] A. Alton,[64,*] G. Alverson,[63] G. A. Alves,[2] M. Anastasoaie,[34] L. S. Ancu,[34] T. Andeen,[53] S. Anderson,[45] B. Andrieu,[16] M. S. Anzelc,[53] Y. Arnoud,[13] M. Arov,[52] A. Askew,[49] B. Åsman,[40] A. C. S. Assis Jesus,[3] O. Atramentov,[49] C. Autermann,[20] C. Avila,[7] C. Ay,[23] F. Badaud,[12] A. Baden,[61] L. Bagby,[52] B. Baldin,[50] D. V. Bandurin,[59] P. Banerjee,[28] S. Banerjee,[28] E. Barberis,[63] P. Bargassa,[80] P. Baringer,[58] C. Barnes,[43] J. Barreto,[2] J. F. Bartlett,[50] U. Bassler,[16] D. Bauer,[43] S. Beale,[5] A. Bean,[58] M. Begalli,[3] M. Begel,[71] C. Belanger-Champagne,[40] L. Bellantoni,[50] A. Bellavance,[67] J. A. Benitez,[65] S. B. Beri,[26] G. Bernardi,[16] R. Bernhard,[22] L. Berntzon,[14] I. Bertram,[42] M. Besançon,[17] R. Beuselinck,[43] V. A. Bezzubov,[38] P. C. Bhat,[50] V. Bhatnagar,[26] M. Binder,[24] C. Biscarat,[19] I. Blackler,[43] G. Blazey,[52] F. Blekman,[43] S. Blessing,[49] D. Bloch,[18] K. Bloom,[67] A. Boehnlein,[50] D. Boline,[62] T. A. Bolton,[59] G. Borissov,[42] K. Bos,[33] T. Bose,[77] A. Brandt,[78] R. Brock,[65] G. Brooijmans,[70] A. Bross,[50] D. Brown,[78] N. J. Buchanan,[49] D. Buchholz,[53] M. Buehler,[81] V. Buescher,[22] S. Burdin,[50] S. Burke,[45] T. H. Burnett,[82] E. Busato,[16] C. P. Buszello,[43] J. M. Butler,[62] P. Calfayan,[24] S. Calvet,[14] J. Cammin,[71] S. Caron,[33] W. Carvalho,[3] B. C. K. Casey,[77] N. M. Cason,[55] H. Castilla-Valdez,[32] S. Chakrabarti,[17] D. Chakraborty,[52] K. M. Chan,[71] A. Chandra,[48] F. Charles,[18] E. Cheu,[45] F. Chevallier,[13] D. K. Cho,[62] S. Choi,[31] B. Choudhary,[27] L. Christofek,[77] D. Claes,[67] B. Clément,[18] C. Clément,[40] Y. Coadou,[5] M. Cooke,[80] W. E. Cooper,[50] M. Corcoran,[80] F. Couderc,[17] M.-C. Cousinou,[14] B. Cox,[44] S. Crépé-Renaudin,[13] D. Cutts,[77] M. Ćwiok,[29] H. da Motta,[2] A. Das,[62] M. Das,[60] B. Davies,[42] G. Davies,[43] K. De,[78] P. de Jong,[33] S. J. de Jong,[34] E. De La Cruz-Burelo,[64] C. De Oliveira Martins,[3] J. D. Degenhardt,[64] F. Déliot,[17] M. Demarteau,[50] R. Demina,[71] D. Denisov,[50] S. P. Denisov,[38] S. Desai,[50] H. T. Diehl,[50] M. Diesburg,[50] M. Doidge,[42] A. Dominguez,[67] H. Dong,[72] L. V. Dudko,[37] L. Duflot,[15] S. R. Dugad,[28] D. Duggan,[49] A. Duperrin,[14] J. Dyer,[65] A. Dyshkant,[52] M. Eads,[67] D. Edmunds,[65] J. Ellison,[48] V. D. Elvira,[50] Y. Enari,[77] S. Eno,[61] P. Ermolov,[37] H. Evans,[54] A. Evdokimov,[36] V. N. Evdokimov,[38] L. Feligioni,[62] A. V. Ferapontov,[59] T. Ferbel,[71] F. Fiedler,[24] F. Filthaut,[34] W. Fisher,[50] H. E. Fisk,[50] M. Ford,[44] M. Fortner,[52] H. Fox,[22] S. Fu,[50] S. Fuess,[50] T. Gadfort,[82] C. F. Galea,[34] E. Gallas,[50] E. Galyaev,[55] C. Garcia,[71] A. Garcia-Bellido,[82] V. Gavrilov,[36] A. Gay,[18] P. Gay,[12] W. Geist,[18] D. Gelé,[18] R. Gelhaus,[48] C. E. Gerber,[51] Y. Gershtein,[49] D. Gillberg,[5] G. Ginther,[71] N. Gollub,[40] B. Gómez,[7] A. Goussiou,[55] P. D. Grannis,[72] H. Greenlee,[50] Z. D. Greenwood,[60] E. M. Gregores,[4] G. Grenier,[19] Ph. Gris,[12] J.-F. Grivaz,[15] A. Grohsjean,[24] S. Grünendahl,[50] M. W. Grünewald,[29] F. Guo,[72] J. Guo,[72] G. Gutierrez,[50] P. Gutierrez,[75] A. Haas,[70] N. J. Hadley,[61] P. Haefner,[24] S. Hagopian,[49] J. Haley,[68] I. Hall,[75] R. E. Hall,[47] L. Han,[6] K. Hanagaki,[50] P. Hansson,[40] K. Harder,[44] A. Harel,[71] R. Harrington,[63] J. M. Hauptman,[57] R. Hauser,[65] J. Hays,[43] T. Hebbeker,[20] D. Hedin,[52] J. G. Hegeman,[33] J. M. Heinmiller,[51] A. P. Heinson,[48] U. Heintz,[62] C. Hensel,[58] K. Herner,[72] G. Hesketh,[63] M. D. Hildreth,[55] R. Hirosky,[81] J. D. Hobbs,[72] B. Hoeneisen,[11] H. Hoeth,[25] M. Hohlfeld,[15] S. J. Hong,[30] R. Hooper,[77] P. Houben,[33] Y. Hu,[72] Z. Hubacek,[9] V. Hynek,[8] I. Iashvili,[69] R. Illingworth,[50] A. S. Ito,[50] S. Jabeen,[62] M. Jaffré,[15] S. Jain,[75] K. Jakobs,[22] C. Jarvis,[61] A. Jenkins,[43] R. Jesik,[43] K. Johns,[45] C. Johnson,[70] M. Johnson,[50] A. Jonckheere,[50] P. Jonsson,[43] A. Juste,[50] D. Käfer,[20] S. Kahn,[73] E. Kajfasz,[14] A. M. Kalinin,[35] J. M. Kalk,[60] J. R. Kalk,[65] S. Kappler,[20] D. Karmanov,[37] J. Kasper,[62] P. Kasper,[50] I. Katsanos,[70] D. Kau,[49] R. Kaur,[26] R. Kehoe,[79] S. Kermiche,[14] N. Khalatyan,[62] A. Khanov,[76] A. Kharchilava,[69] Y. M. Kharzheev,[35] D. Khatidze,[70] H. Kim,[31] T. J. Kim,[30] M. H. Kirby,[34] B. Klima,[50] J. M. Kohli,[26] J.-P. Konrath,[22] M. Kopal,[75] V. M. Korablev,[38] J. Kotcher,[73] B. Kothari,[70] A. Koubarovsky,[37] A. V. Kozelov,[38] D. Krop,[54] A. Kryemadhi,[81] T. Kuhl,[23] A. Kumar,[69] S. Kunori,[61] A. Kupco,[10] T. Kurča,[19] J. Kvita,[8] D. Lam,[55] S. Lammers,[70] G. Landsberg,[77] J. Lazoflores,[49] A.-C. Le Bihan,[18] P. Lebrun,[19] W. M. Lee,[50] A. Leflat,[37] F. Lehner,[41] V. Lesne,[12] J. Leveque,[45] P. Lewis,[43] J. Li,[78] L. Li,[48] Q. Z. Li,[50] S. M. Lietti,[4] J. G. R. Lima,[52] D. Lincoln,[50] J. Linnemann,[65] V. V. Lipaev,[38] R. Lipton,[50] Z. Liu,[5] L. Lobo,[43] A. Lobodenko,[39] M. Lokajicek,[10] P. Love,[42] H. J. Lubatti,[82] M. Lynker,[55] A. L. Lyon,[50] A. K. A. Maciel,[2] R. J. Madaras,[46] P. Mättig,[25] C. Magass,[20] A. Magerkurth,[64] N. Makovec,[15] P. K. Mal,[55] H. B. Malbouisson,[3] S. Malik,[67] V. L. Malyshev,[35] H. S. Mao,[50] Y. Maravin,[59] R. McCarthy,[72] A. Melnitchouk,[66] A. Mendes,[14] L. Mendoza,[7] P. G. Mercadante,[4] M. Merkin,[37] K. W. Merritt,[50] A. Meyer,[20] J. Meyer,[21] M. Michaut,[17] H. Miettinen,[80] T. Millet,[19] J. Mitrevski,[70] J. Molina,[3] R. K. Mommsen,[44] N. K. Mondal,[28] J. Monk,[44] R. W. Moore,[5] T. Moulik,[58] G. S. Muanza,[19] M. Mulders,[50] M. Mulhearn,[70] O. Mundal,[22] L. Mundim,[3] E. Nagy,[14] M. Naimuddin,[27] M. Narain,[62] N. A. Naumann,[34] H. A. Neal,[64] J. P. Negret,[7] P. Neustroev,[39] C. Noeding,[22] A. Nomerotski,[50] S. F. Novaes,[4] T. Nunnemann,[24] V. O'Dell,[50] D. C. O'Neil,[5] G. Obrant,[39] C. Ochando,[15] V. Oguri,[3] N. Oliveira,[3] D. Onoprienko,[59] N. Oshima,[50] J. Osta,[55] R. Otec,[9] G. J. Otero y Garzón,[51] M. Owen,[44] P. Padley,[80] M. Pangilinan,[62] N. Parashar,[56]

S.-J. Park,[71] S. K. Park,[30] J. Parsons,[70] R. Partridge,[77] N. Parua,[72] A. Patwa,[73] G. Pawloski,[80] P. M. Perea,[48] K. Peters,[44] Y. Peters,[25] P. Pétroff,[15] M. Petteni,[43] R. Piegaia,[1] J. Piper,[65] M.-A. Pleier,[21] P. L. M. Podesta-Lerma,[32] V. M. Podstavkov,[50] Y. Pogorelov,[55] M.-E. Pol,[2] A. Pompoš,[75] B. G. Pope,[65] A. V. Popov,[38] C. Potter,[5] W. L. Prado da Silva,[3] H. B. Prosper,[49] S. Protopopescu,[73] J. Qian,[64] A. Quadt,[21] B. Quinn,[66] M. S. Rangel,[2] K. J. Rani,[28] K. Ranjan,[27] P. N. Ratoff,[42] P. Renkel,[79] S. Reucroft,[63] M. Rijssenbeek,[72] I. Ripp-Baudot,[18] F. Rizatdinova,[76] S. Robinson,[43] R. F. Rodrigues,[3] C. Royon,[17] P. Rubinov,[50] R. Ruchti,[55] G. Sajot,[13] A. Sánchez-Hernández,[32] M. P. Sanders,[16] A. Santoro,[3] G. Savage,[50] L. Sawyer,[60] T. Scanlon,[43] D. Schaile,[24] R. D. Schamberger,[72] Y. Scheglov,[39] H. Schellman,[53] P. Schieferdecker,[24] C. Schmitt,[25] C. Schwanenberger,[44] A. Schwartzman,[68] R. Schwienhorst,[65] J. Sekaric,[49] S. Sengupta,[49] H. Severini,[75] E. Shabalina,[51] M. Shamim,[59] V. Shary,[17] A. A. Shchukin,[38] R. K. Shivpuri,[27] D. Shpakov,[50] V. Siccardi,[18] R. A. Sidwell,[59] V. Simak,[9] V. Sirotenko,[50] P. Skubic,[75] P. Slattery,[71] R. P. Smith,[50] G. R. Snow,[67] J. Snow,[74] S. Snyder,[73] S. Söldner-Rembold,[44] X. Song,[52] L. Sonnenschein,[16] A. Sopczak,[42] M. Sosebee,[78] K. Soustruznik,[8] M. Souza,[2] B. Spurlock,[78] J. Stark,[13] J. Steele,[60] V. Stolin,[36] A. Stone,[51] D. A. Stoyanova,[38] J. Strandberg,[64] S. Strandberg,[40] M. A. Strang,[69] M. Strauss,[75] R. Ströhmer,[24] D. Strom,[53] M. Strovink,[46] L. Stutte,[50] S. Sumowidagdo,[49] P. Svoisky,[55] A. Sznajder,[3] M. Talby,[14] P. Tamburello,[45] W. Taylor,[5] P. Telford,[44] J. Temple,[45] B. Tiller,[24] M. Titov,[22] V. V. Tokmenin,[35] M. Tomoto,[50] T. Toole,[61] I. Torchiani,[22] T. Trefzger,[23] S. Trincaz-Duvoid,[16] D. Tsybychev,[72] B. Tuchming,[17] C. Tully,[68] P. M. Tuts,[70] R. Unalan,[65] L. Uvarov,[39] S. Uvarov,[39] S. Uzunyan,[52] B. Vachon,[5] P. J. van den Berg,[33] B. van Eijk,[35] R. Van Kooten,[54] W. M. van Leeuwen,[33] N. Varelas,[51] E. W. Varnes,[45] A. Vartapetian,[78] I. A. Vasilyev,[38] M. Vaupel,[25] P. Verdier,[19] L. S. Vertogradov,[35] M. Verzocchi,[50] F. Villeneuve-Seguier,[43] P. Vint,[43] J.-R. Vlimant,[16] E. Von Toerne,[59] M. Voutilainen,[67,†] M. Vreeswijk,[33] H. D. Wahl,[49] L. Wang,[61] M. H. L. S. Wang,[50] J. Warchol,[55] G. Watts,[82] M. Wayne,[55] G. Weber,[23] M. Weber,[50] H. Weerts,[65] N. Wermes,[21] M. Wetstein,[61] A. White,[78] D. Wicke,[25] G. W. Wilson,[58] S. J. Wimpenny,[48] M. Wobisch,[50] J. Womersley,[50] D. R. Wood,[63] T. R. Wyatt,[44] Y. Xie,[77] S. Yacoob,[53] R. Yamada,[50] M. Yan,[61] T. Yasuda,[50] Y. A. Yatsunenko,[35] K. Yip,[73] H. D. Yoo,[77] S. W. Youn,[53] C. Yu,[13] J. Yu,[78] A. Yurkewicz,[72] A. Zatserklyaniy,[52] C. Zeitnitz,[25] D. Zhang,[50] T. Zhao,[82] B. Zhou,[64] J. Zhu,[72] M. Zielinski,[71] D. Zieminska,[54] A. Zieminski,[54] V. Zutshi,[52] and E. G. Zverev[37]

(D0 Collaboration)

[1]*Universidad de Buenos Aires, Buenos Aires, Argentina*
[2]*LAFEX, Centro Brasileiro de Pesquisas Físicas, Rio de Janeiro, Brazil*
[3]*Universidade do Estado do Rio de Janeiro, Rio de Janeiro, Brazil*
[4]*Instituto de Física Teórica, Universidade Estadual Paulista, São Paulo, Brazil*
[5]*University of Alberta, Edmonton, Alberta, Canada,*
Simon Fraser University, Burnaby, British Columbia, Canada,
York University, Toronto, Ontario, Canada,
and McGill University, Montreal, Quebec, Canada
[6]*University of Science and Technology of China, Hefei, People's Republic of China*
[7]*Universidad de los Andes, Bogotá, Colombia*
[8]*Center for Particle Physics, Charles University, Prague, Czech Republic*
[9]*Czech Technical University, Prague, Czech Republic*
[10]*Center for Particle Physics, Institute of Physics, Academy of Sciences of the Czech Republic, Prague, Czech Republic*
[11]*Universidad San Francisco de Quito, Quito, Ecuador*
[12]*Laboratoire de Physique Corpusculaire, IN2P3-CNRS, Université Blaise Pascal, Clermont-Ferrand, France*
[13]*Laboratoire de Physique Subatomique et de Cosmologie, IN2P3-CNRS, Universite de Grenoble 1, Grenoble, France*
[14]*CPPM, IN2P3-CNRS, Université de la Méditerranée, Marseille, France*
[15]*Laboratoire de l'Accélérateur Linéaire, IN2P3-CNRS et Université Paris-Sud, Orsay, France*
[16]*LPNHE, IN2P3-CNRS, Universités Paris VI and VII, Paris, France*
[17]*DAPNIA/Service de Physique des Particules, CEA, Saclay, France*
[18]*IPHC, IN2P3-CNRS, Université Louis Pasteur, Strasbourg, France,*
and Université de Haute Alsace, Mulhouse, France
[19]*Institut de Physique Nucléaire de Lyon, IN2P3-CNRS, Université Claude Bernard, Villeurbanne, France*
[20]*III. Physikalisches Institut A, RWTH Aachen, Aachen, Germany*
[21]*Physikalisches Institut, Universität Bonn, Bonn, Germany*
[22]*Physikalisches Institut, Universität Freiburg, Freiburg, Germany*
[23]*Institut für Physik, Universität Mainz, Mainz, Germany*
[24]*Ludwig-Maximilians-Universität München, München, Germany*
[25]*Fachbereich Physik, University of Wuppertal, Wuppertal, Germany*

^{26}Panjab University, Chandigarh, India
^{27}Delhi University, Delhi, India
^{28}Tata Institute of Fundamental Research, Mumbai, India
^{29}University College Dublin, Dublin, Ireland
^{30}Korea Detector Laboratory, Korea University, Seoul, Korea
^{31}SungKyunKwan University, Suwon, Korea
^{32}CINVESTAV, Mexico City, Mexico
^{33}FOM-Institute NIKHEF, Amsterdam, The Netherlands
and University of Amsterdam/NIKHEF, Amsterdam, The Netherlands
^{34}Radboud University Nijmegen/NIKHEF, Nijmegen, The Netherlands
^{35}Joint Institute for Nuclear Research, Dubna, Russia
^{36}Institute for Theoretical and Experimental Physics, Moscow, Russia
^{37}Moscow State University, Moscow, Russia
^{38}Institute for High Energy Physics, Protvino, Russia
^{39}Petersburg Nuclear Physics Institute, St. Petersburg, Russia
^{40}Lund University, Lund, Sweden, Royal Institute of Technology and Stockholm University, Stockholm, Sweden
and Uppsala University, Uppsala, Sweden
^{41}Physik Institut der Universität Zürich, Zürich, Switzerland
^{42}Lancaster University, Lancaster, United Kingdom
^{43}Imperial College, London, United Kingdom
^{44}University of Manchester, Manchester, United Kingdom
^{45}University of Arizona, Tucson, Arizona 85721, USA
^{46}Lawrence Berkeley National Laboratory, Berkeley, California 94720, USA
and University of California, Berkeley, California 94720, USA
^{47}California State University, Fresno, California 93740, USA
^{48}University of California, Riverside, California 92521, USA
^{49}Florida State University, Tallahassee, Florida 32306, USA
^{50}Fermi National Accelerator Laboratory, Batavia, Illinois 60510, USA
^{51}University of Illinois at Chicago, Chicago, Illinois 60607, USA
^{52}Northern Illinois University, DeKalb, Illinois 60115, USA
^{53}Northwestern University, Evanston, Illinois 60208, USA
^{54}Indiana University, Bloomington, Indiana 47405, USA
^{55}University of Notre Dame, Notre Dame, Indiana 46556, USA
^{56}Purdue University Calumet, Hammond, Indiana 46323, USA
^{57}Iowa State University, Ames, Iowa 50011, USA
^{58}University of Kansas, Lawrence, Kansas 66045, USA
^{59}Kansas State University, Manhattan, Kansas 66506, USA
^{60}Louisiana Tech University, Ruston, Louisiana 71272, USA
^{61}University of Maryland, College Park, Maryland 20742, USA
^{62}Boston University, Boston, Massachusetts 02215, USA
^{63}Northeastern University, Boston, Massachusetts 02115, USA
^{64}University of Michigan, Ann Arbor, Michigan 48109, USA
^{65}Michigan State University, East Lansing, Michigan 48824, USA
^{66}University of Mississippi, University, Mississippi 38677, USA
^{67}University of Nebraska, Lincoln, Nebraska 68588, USA
^{68}Princeton University, Princeton, New Jersey 08544, USA
^{69}State University of New York, Buffalo, New York 14260, USA
^{70}Columbia University, New York, New York 10027, USA
^{71}University of Rochester, Rochester, New York 14627, USA
^{72}State University of New York, Stony Brook, New York 11794, USA
^{73}Brookhaven National Laboratory, Upton, New York 11973, USA
^{74}Langston University, Langston, Oklahoma 73050, USA
^{75}University of Oklahoma, Norman, Oklahoma 73019, USA
^{76}Oklahoma State University, Stillwater, Oklahoma 74078, USA
^{77}Brown University, Providence, Rhode Island 02912, USA
^{78}University of Texas, Arlington, Texas 76019, USA
^{79}Southern Methodist University, Dallas, Texas 75275, USA

*Visitor from Augustana College, Sioux Falls, SD, USA
†Visitor from Helsinki Institute of Physics, Helsinki, Finland.

[80]*Rice University, Houston, Texas 77005, USA*
[81]*University of Virginia, Charlottesville, Virginia 22901, USA*
[82]*University of Washington, Seattle, Washington 98195, USA*

A measurement of the top quark pair production cross section in proton antiproton collisions at an interaction energy of $\sqrt{s} = 1.96$ TeV is presented. This analysis uses 405 ± 25 pb^{-1} of data collected with the D0 detector at the Fermilab Tevatron Collider. Fully hadronic $t\bar{t}$ decays with final states of six or more jets are separated from the multijet background using secondary vertex tagging and a neural network. The $t\bar{t}$ cross section is measured as $\sigma_{t\bar{t}} = 4.5^{+2.0}_{-1.9}(\text{stat})^{+1.4}_{-1.1}(\text{syst}) \pm 0.3(\text{lumi})$ pb for a top quark mass of $m_t = 175$ GeV/c^2.

The standard model (SM) predicts that the top quark decays primarily into a W boson and a b quark. The measurement presented here tests the prediction of the SM in proton antiproton collisions at an interaction energy of $\sqrt{s} = 1.96$ TeV. The measurement is performed in the dominant decay mode of the $t\bar{t}$ system: when both W bosons decay to quarks, the so-called fully hadronic decay channel. This topology occurs in 46% of $t\bar{t}$ events. The theoretical signature for fully hadronic $t\bar{t}$ events is six or more jets originating from the hadronization of the six quarks. Of the six jets, two originate from b quark decays. Fully hadronic $t\bar{t}$ events are difficult to identify at hadron colliders because the background rate is many orders of magnitude larger than that of the $t\bar{t}$ signal.

We report a measurement of the production cross section of top quark pairs, $\sigma_{t\bar{t}}$, that exploits the long lifetime of the b hadrons in identifying b jets, using data collected with D0 in the fully hadronic channel. To increase the sensitivity for $t\bar{t}$ events, we used a neural network to distinguish the signal from the overwhelming background of multijet production through quantum chromodynamic processes (QCD).

The D0 detector [1] has a central tracking system consisting of a silicon micro strip tracker (SMT) and a central fiber tracker (CFT), both located within a 2 T superconducting solenoidal magnet, with designs optimized for tracking and vertexing at pseudorapidities $|\eta| < 3$ and $|\eta| < 2.5$, respectively. Rapidity y and pseudorapidity η are defined as functions of the polar angle θ and parameter β as $y(\theta, \beta) = \frac{1}{2} \ln[(1 + \beta \cos\theta)/(1 - \beta \cos\theta)]$ and $\eta(\theta) = y(\theta, 1)$, where β is the ratio of the particle's momentum to its energy. The liquid-argon and uranium calorimeter has a central section (CC) covering pseudorapidities $|\eta|$ up to ≈ 1.1 and two end calorimeters (EC) that extend coverage to $|\eta| \approx 4.2$, with all three housed in separate cryostats. Each calorimeter cryostat contains a multilayer electromagnetic calorimeter, a finely segmented hadronic calorimeter and a third hadronic calorimeter that is more coarsely segmented, providing both segmentation in depth and in projective towers of size 0.1×0.1 in η-ϕ space, where ϕ is the azimuthal angle in radians. An outer muon system, covering $|\eta| < 2$, consists of a layer of tracking detectors and scintillation trigger counters in front of 1.8 T iron toroids, followed by two similar layers after the toroids. The luminosity is measured using plastic scintillator arrays placed in front of the EC cryostats.

The data set was collected between 2002 and 2004 and corresponds to an integrated luminosity $\mathcal{L} = 405 \pm 25$ pb^{-1} [2]. To isolate events with six jets, we used a dedicated multijet trigger. The requirements on the trigger, particularly on jet and trigger tower energy thresholds, were tightened during the collection of the data set to manage the increasing instantaneous luminosities delivered by the Fermilab Tevatron Collider. The change in trigger requirements had little effect on the efficiency for signal, while removing an increasing number of background events [3]. The trigger was tuned for the fully hadronic $t\bar{t}$ channel and was optimized to remain as efficient as possible while using limited bandwidth. The collection rate after all trigger levels was fixed to a few Hz, which was completely dominated by QCD multijet events as the hadronic $t\bar{t}$ event production rate is expected to be a few events per day. We required three or four trigger towers above a transverse energy threshold of 5 GeV at the first trigger level, three reconstructed jets with transverse energies (E_T) above 8 GeV at the second trigger level, combined with a requirement on the sum of the transverse momenta (p_T) of the jets, and four or five reconstructed jets at transverse energy thresholds between 10 and 30 GeV at the highest trigger level [1].

We simulated $t\bar{t}$ production using ALPGEN 1.3 to generate the parton-level processes and PYTHIA 6.2 to model hadronization [4,5]. We used a top quark mass of $m_t = 175$ GeV/c^2. The decay of hadrons carrying bottom quarks was modeled using EVTGEN [6]. The simulated $t\bar{t}$ events were processed with the full GEANT-based D0 detector simulation, after which the Monte Carlo (MC) events were passed through the same reconstruction program as was used for data. The differences between the MC model and the data were very small and were corrected using factors derived from detailed comparisons between the MC model and the data for well understood SM processes such as the jets in Z boson and QCD dijet production.

In the offline analysis, jets were defined with an iterative cone algorithm [7]. Before the jet algorithm was applied, calorimeter noise was suppressed by removing isolated cells whose measured energy was lower than 4 standard deviations above cell pedestal. In the case that a cell above this threshold was found to be adjacent to one with an energy less than 4 standard deviations above pedestal, the latter was retained if its signal exceeded 2.5 standard deviations above pedestal. Cells that were reconstructed with negative energies were always removed.

The elements for cone jet reconstruction consisted of projective towers of calorimeter cells. First, seeds were defined using a preclustering algorithm, using calorimeter towers above an energy threshold of 0.5 GeV. The cone jet reconstruction, an iterative clustering process where the jet axis was required to match the axis of a projective cone, was then run using all preclusters above 1.0 GeV as seeds. As jets from $t\bar{t}$ production are relatively narrow due to relatively high jet p_T, the jets were defined using a cone with radius $R_{cone} = 0.5$, where $\Delta R = \sqrt{(\Delta y)^2 + (\Delta \phi)^2}$. The resulting jets (proto-jets) took into account all energy deposits contained in the jet cone. If two proto-jets were within $1 < \Delta R/R_{cone} < 2$, an additional midpoint clustering was applied, where the combination of the two proto-jets was used as a seed for a possible additional proto-jet. At this stage, the proto-jets that share transverse momentum were examined with a splitting and merging algorithm, after which each calorimeter tower was assigned to one proto-jet at most. The proto-jets were merged if the shared p_T exceeded 50% of the p_T of the proto-jet with the lowest transverse momentum and the towers were added to the most energetic proto-jet while the other candidate was rejected. If the proto-jets shared less than half of their p_T, the shared towers were individually assigned to the proto-jet which was closest in ΔR space. The collection of stable proto-jets remaining was then referred to as the *reconstructed* jets in the event. The minimal p_T of a reconstructed jet was required to be 8 GeV/c before any energy corrections were applied.

We removed jets caused by electromagnetic particles and jets resulting from noise in hadronic sections of the calorimeter by requiring that the fraction of the jet energy deposited in the calorimeter was between 0.05 and 0.95 and the fraction of energy in the coarse hadronic calorimeter was less than 0.4. Jets formed from clusters of calorimeter cells known to be affected by noise were also rejected. The remaining noise contribution was removed by requiring that the jet also satisfied the first level trigger requirements.

To correct the calorimeter jet energies back to the level of particle jets, a jet energy scale (JES) correction C^{JES} was applied. The same procedure has to be applied to Monte Carlo jets to ensure an identical calorimeter response in data and simulation. The particle level or true jet energy E^{true} was obtained from the measured jet energy E^m and the detector pseudorapidity, measured from the center of the detector (η_{det}), using the relation

$$E^{true} = \frac{E^m - E_0(\eta_{det}, \mathcal{L})}{\mathcal{R}(\eta_{det}, E^m) S(\eta_{det}, E^m)} = C^{JES}(E^m, \eta_{det}, \mathcal{L}) \cdot E^m.$$

$$(1)$$

In data and MC the total correction was applied to the measured energy E^m as a multiplicative factor C^{JES}. $E_0(\eta_{det}, \mathcal{L})$ was the offset energy created by electronics noise and noise signal caused by the uranium in the calorimeter, pile-up energy from previous collisions, and the additional energy from the underlying physics event. The dependence on the luminosity $\mathcal{L}$ was caused by the fact that the number of additional interactions was dependent on the instantaneous luminosity, while the dependence on y was caused by variations in the calorimeter occupancy as a function of the jet rapidity. $\mathcal{R}(\eta_{det}, E^m)$ parameterized the energy response of the calorimeter, while $S(\eta_{det}, E^m)$ represents the fraction of the true particle jet energy that was deposited inside the jet cone. This out-of-cone showering correction depended on the energy of the jet and its location in the calorimeter.

The JES was measured directly in photon + jet events, which are quark dominated (like $t\bar{t}$). The method was identical for data and simulation and used transverse momentum balancing between the jet and the photon. As the energy scale of the photon was directly and precisely measured (the electromagnetic calorimeter response was derived from measurements of resonances in the $e^+ e^-$ spectrum like the Z boson), the true jet energy could be derived from the difference between the photon and jet transverse momentum. E_0, $\mathcal{R}$, and S were fit as a function of jet rapidity and measured energy, which lead to uncertainties coming from the fit (statistical) and the method (systematic). The total correction C^{JES} was approximately 1.4 for data jets in the energy range expected for jets associated with top quark events. The corrections for data and Monte Carlo simulation are in good agreement and the used systematic uncertainty cover for any possible difference in scale. The systematic uncertainties on C^{JES} were of the order of a few percent and depended on the jet energy and rapidity.

The jet energy resolution was measured in photon + jet data for low jet energies and dijet data for higher jet energy values. Fits to the transverse energy asymmetry $[p_T(1) - p_T(2)]/[p_T(1) + p_T(2)]$ between the transverse momenta of the back-to-back jets and/or photon $[p_T(1)$ and $p_T(2)]$ were then used to obtain the jet energy resolution as a function of jet rapidity and transverse energy. The uncertainties on the jet energy resolution were dominated by limited statistics in the samples used.

In this analysis, we considered a data set consisting of events with four or more reconstructed jets, in which the scalar sum of the uncorrected transverse momenta H_T^{uncorr} of all the jets in the event was greater than 90 GeV/c. The final analysis sample was a subset of this sample, where at

least six jets with corrected transverse momentum greater than 15 GeV/c and $|y| < 2.5$ were required. Events with isolated high transverse momentum electron or muon candidates were vetoed to ensure that the all-hadronic and leptonic $t\bar{t}$ samples were disjoint [8,9]. In addition, we rejected events where two distinct $p\bar{p}$ interactions with separate primary vertices were observed and the jets in the event were not assigned to only one of the two primary vertices. The primary vertex requirement did not affect minimum bias interactions or $t\bar{t}$ events. Table I lists the efficiencies after the first set of selection cuts, commonly referred to as preselection, which includes the requirements on the primary vertex, the number of reconstructed jets and the presence of isolated leptons, and the efficiency after preselection and after preselection and the trigger. Besides selecting all-hadronic $t\bar{t}$ events, the analysis was also expected to accept a small contribution from the semileptonic (lepton + jets) $t\bar{t}$ decay channel. The combined efficiency included the fully hadronic and semileptonic W-boson branching fractions of 0.4619 ± 0.0048 and 0.4349 ± 0.0027 respectively [10].

We used a secondary vertex tagging algorithm (SVT) to identify b-quark jets. The algorithm was the same as that used in previously published D0 $t\bar{t}$ production cross section measurements [8,9]. Secondary vertex candidates were reconstructed from two or more tracks in the jet, removing vertices consistent with those having originated from long-lived light hadrons, for example K_S^0 and Λ. Two configurations of the secondary vertex algorithm were used; these were labeled "loose" and "tight," respectively. If a reconstructed secondary vertex in the jet had a transverse decay length L_{xy} significance $(L_{xy}/\sigma_{L_{xy}}) > 5(7)$, the jet was tagged as a loose (tight) b-quark jet. The loose SVT was chosen to efficiently identify b-quark jets, while the tight SVT was configured to accept only very few light-quark jets while sacrificing a small reduction in the efficiency for b-quark jets. Events with two or more loosely tagged jets were called double-tag events. The sample that did not contain two loosely tagged jets was inspected for events with one tight tag. Events thus isolated were labeled single-tag events. The fully exclusive samples of single-tag and double-tag events were treated separately because of their different signal-to-background ratios. The use of the tight SVT selection for single tagged events optimized the re-

jection of mistags; the main background in the single-tag analysis. When two tags were required, the background sample started to be dominated by direct $b\bar{b}$ production. The choice to use the loose SVT optimized the double-tag analysis for signal efficiency instead of background rejection.

Compared to light-quark QCD multijet events, $t\bar{t}$ events on average have more jets of higher energy and with less boost in the beam direction, resulting in events with many central jets that all have similar and relatively high energies. Moreover, the fully hadronic decay makes it possible to reconstruct the W boson and t quark four-momenta. To distinguish between signal and background, we used the following event characteristics [11]:

(i) H_T: The scalar sum of the corrected transverse momenta of the jets (Fig. 1).

(ii) E_T^{56}: The square root of the product of the transverse momenta of the fifth and sixth leading jet (Fig. 2).

(iii) $\mathcal{A}$: The aplanarity as calculated from the normalized momentum tensor (Fig. 3) [8,9,11].

(iv) $\langle \eta^2 \rangle$: The p_T-weighted mean square of the y of the jets in an event (Fig. 4), see also Ref. [11].

(v) $\mathcal{M}$: The mass-χ^2 variable, which was defined as $\mathcal{M} = (M_{W_1} - M_W)^2/\sigma_{M_W}^2 + (M_{W_2} - M_W)^2/\sigma_{M_W}^2 + (m_{t_1} - m_{t_2})^2/\sigma_{m_t}^2$, where the parameters M_W, σ_{M_W}, and σ_{m_t} were the invariant mass and mass resolution from the jet four-momenta calculated as observed in all-hadronic $t\bar{t}$ MC, respectively, 79, 11, and 21 GeV/c^2 after all corrections and resolutions were included [12]. M_{W_i} and m_{t_i} were calculated for every possible permutation of the jets in the event. We did not distinguish between tagged and untagged jets. The combination of jets that yielded the lowest value of $\mathcal{M}$ is used (Fig. 5).

(vi) M_{min}^{34}: The second-smallest dijet mass in the event. First, all possible dijet masses were considered and the jets that yield the smallest mass were rejected. M_{min}^{34} was the smallest dijet mass as found from the remaining jets (Fig. 6).

The top quark production cross section was calculated from the output of NN, an artificial neural network trained to force its output near 1 for $t\bar{t}$ events and near -1 for QCD multijet events, using the multilayer perceptron in the ROOT analysis program [13]. The six parameters illustrated in

TABLE I. Efficiency for selection criteria applied before b-jet identification. Efficiencies listed include the efficiency for all previous selection criteria. The trigger efficiency is quoted for events that have passed the preselection. The uncertainties are due to Monte Carlo statistics. Listed are the selection efficiencies as determined for $t\bar{t}$ in the hadronic decay channel, the lepton + jets decay channel, and the efficiency for all different decay channels corrected for W boson branching fractions.

Cut	$t\bar{t} \rightarrow$ hadrons	$t\bar{t} \rightarrow \ell +$ jets	Any $t\bar{t}$
Preselection	0.2706 ± 0.0016	0.0311 ± 0.0008	0.1385 ± 0.0011
Trigger	0.2527 ± 0.0015	0.0268 ± 0.0007	0.1284 ± 0.0010

Figs. 1–6 were used as input for the neural net. The input parameters were shown to be correlated in dedicated studies used to select appropriate input for NN, where many different quantities were considered. The correlation between the six quantities was observed to be smaller than $|0.20|$, while the most powerful quantity for the discrimination between signal and background was observed to be H_T. The very large background-to-signal ratio in the untagged data allowed us to use untagged data as background input for the training of NN, while $t\bar{t}$ MC was used for the
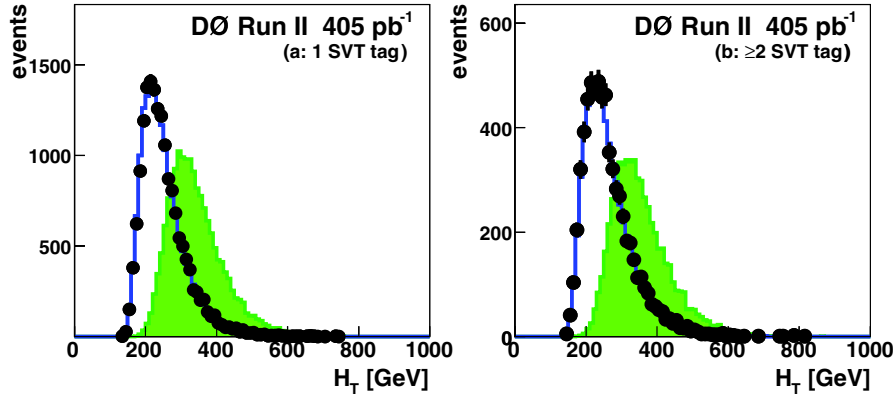
FIG. 1 (color online). The H_T distribution for single-tag events (a) and double-tag events (b). Shown are the data (points), the background (solid line), and the expected $t\bar{t}$ distribution (filled histogram) multiplied by 140 (60) for the single (double)-tag analysis.
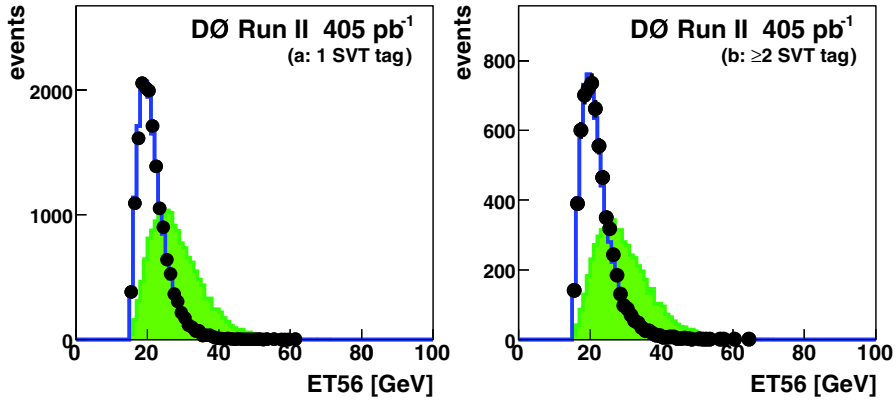
FIG. 2 (color online). The E_T^{56} distribution for single-tag events (a) and double-tag events (b). Shown are the data (points), the background (solid line), and the expected $t\bar{t}$ distribution (filled histogram) multiplied by 140 (60) for the single (double)-tag analysis.
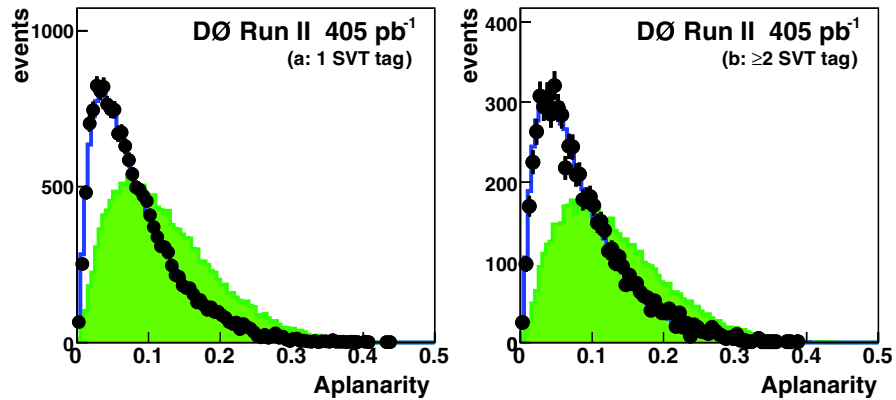
FIG. 3 (color online). The $\mathcal{A}$ distribution for single-tag events (a) and double-tag events (b). Shown are the data (points), the background (solid line) and the expected $t\bar{t}$ distribution (filled histogram) multiplied by 140 (60) for the single (double)-tag analysis.

signal. Figure 7 shows the *NN* discriminant for $t\bar{t}$ signal and multijet background. Although the distributions for single- and double-tag events were different due to increased heavy flavor content in the double-tag sample, both samples showed a clear discrimination between signal and background.

The overwhelming background also made it possible to use the entire (tagged and untagged) sample to estimate the
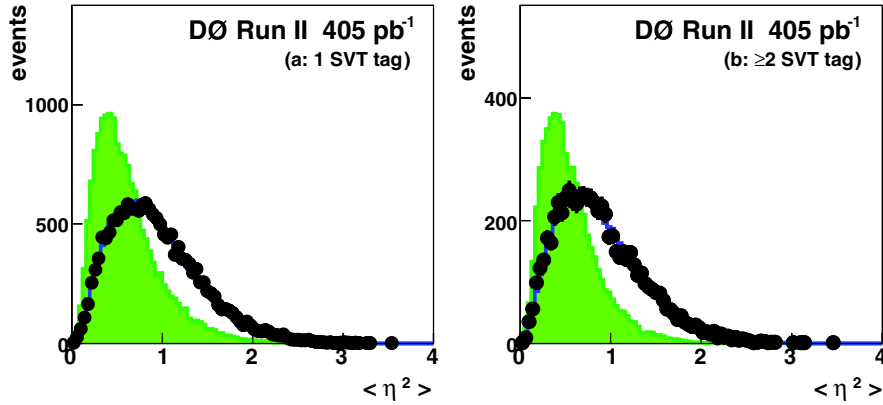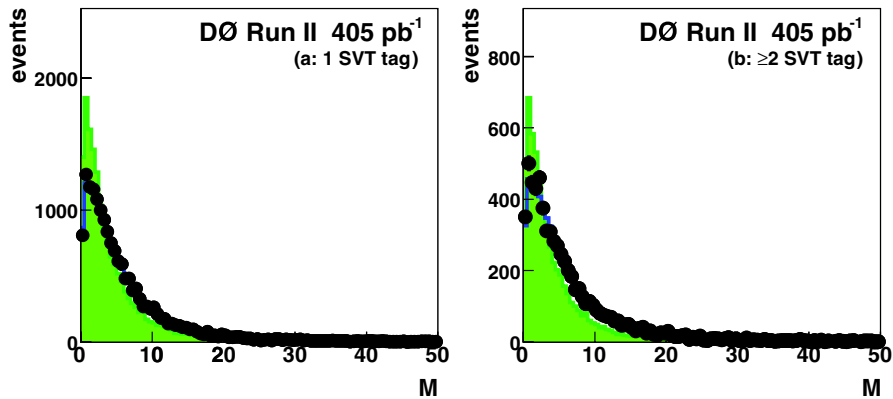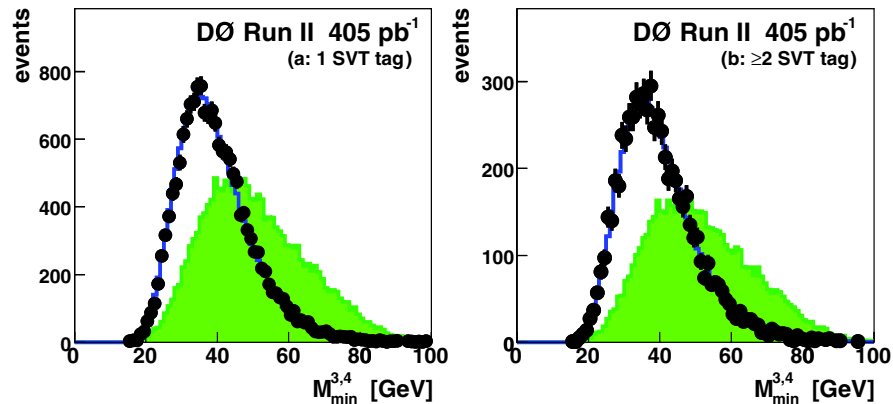

FIG. 4 (color online). The $\langle \eta^2 \rangle$ distribution for single-tag events (a) and double-tag events (b). Shown are the data (points), the background (solid line), and the expected $t\bar{t}$ distribution (filled histogram) multiplied by 140 (60) for the single (double)-tag analysis.


FIG. 5 (color online). The $\mathcal{M}$ distribution for single-tag events (a) and double-tag events (b). Shown are the data (points), the background (solid line), and the expected $t\bar{t}$ distribution (filled histogram) multiplied by 140 (60) for the single (double)-tag analysis.

FIG. 6 (color online). The M_{min}^{34} distribution for single-tag events (a) and double-tag events (b). Shown are the data (points), the background (solid line), and the expected $t\bar{t}$ distribution (filled histogram) multiplied by 140 (60) for the single (double)-tag analysis.
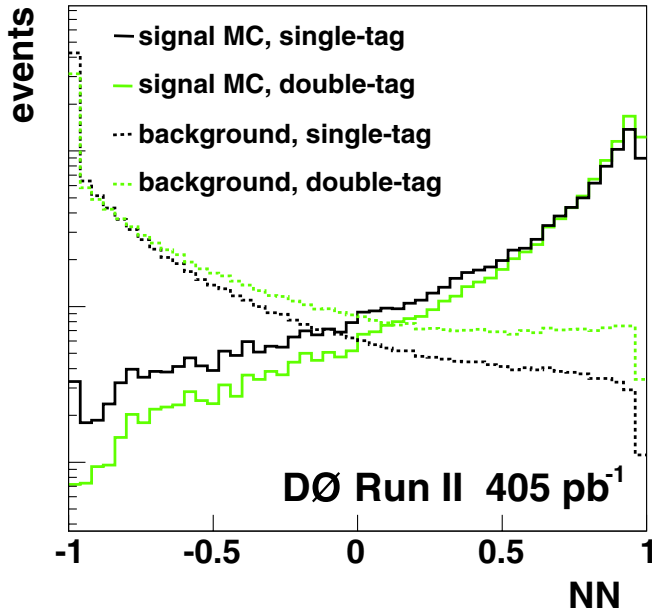
FIG. 7 (color online). The output discriminant of an artificial neural network (*NN*) with six input nodes. All distributions are normalized to area. *NN* is optimized to distinguish between fully hadronic $t\bar{t}$ Monte Carlo events (signal) and the background from multijet production (background) as predicted by the tag rate functions.

FIG. 8 (color online). The performance of the TRF prediction on double-tag events (points), without including the correlation factor C_{ij} (dashed histogram), and including C_{ij} for two different functional parameterizations (solid histograms).

background. For the loose and tight SVT, we derived a tag rate function (TRF—the probability for any individual jet to have a secondary vertex tag) from the data with $N_{\text{tags}} \leq 1$. The TRF was parameterized in terms of the p_T, ϕ, and y of the jet and the coordinate along the beam axis (z) of the primary vertex of the event, z_{PV}, in four different H_T bins. To predict the number of tagged jets in the event, it was necessary to correct for a possible correlation between tagged jets. In the single-tag analysis the correlation factor was negligible, unlike in the double-tag analysis, where the presence of $b\bar{b} +$ jets events in the sample enhanced the correlation correction. We corrected for correlations caused by $b\bar{b}$ background by applying a correlation factor C_{ij}, that was parameterized as a function of the cone distance between the tagged jets, ΔR. Figure 8 shows the number of double-tagged events versus ΔR as observed in data, and the distribution as modeled by the TRF with and without including C_{ij}. We considered significantly different functional forms for the parameterization of C_{ij} and found that the choice of parameterization had little effect on the shape of the modeled background distribution.

The probabilities p_i were used to assign a weight, the probability that the event could have a given number of tags, to every tagged and untagged event in the sample. To ensure the TRF prediction was accurate in the region of phase space outside the "background" peak of the neural network, we used the region $-0.7 < NN < 0.5$ to determine a normalization. In this region of phase space, the $t\bar{t}$ content was negligible. A possible dependence on $t\bar{t}$ con-
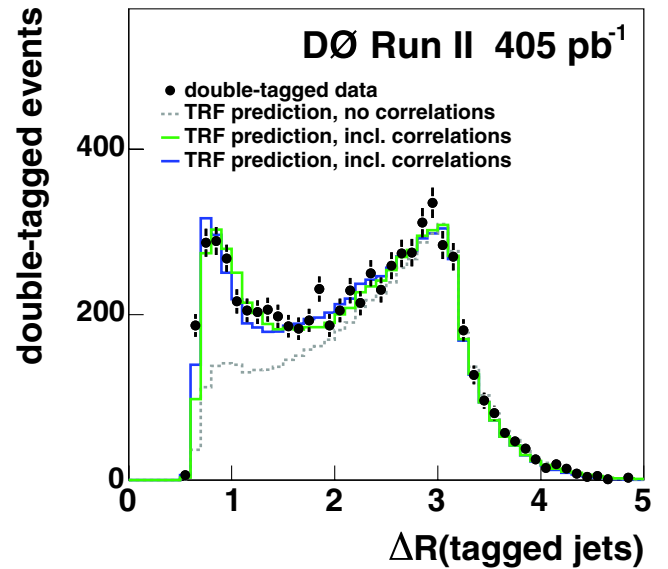
tent was studied by the addition and/or subtraction of simulated $t\bar{t}$ events, as was the variation of the interval used for the normalization. Outside the background peak, the TRF predictions were corrected by $SF_1 = 1.000 \pm 0.009$ for the single-tag analysis and $SF_2 = 0.969 \pm 0.014$ for the double-tag analysis. The errors on the nor-
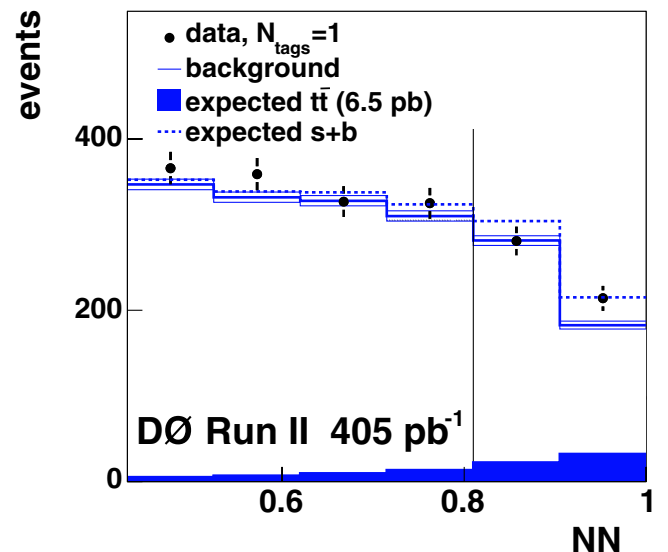

FIG. 9 (color online). The distribution of the *NN* output variable for single-tag events. Shown are the data (points), background (hashed band), signal (filled histogram), and signal + background (dashed histogram). The vertical line represents the used cut of $NN > 0.81$.

malization were taken into account as a systematic uncertainty on the number of background events.

Both the single-tag and the double-tag analysis were expected to be dominated by background, even at large values of *NN*. Figures 9 and 10 show the distribution for data (points), the Monte Carlo simulation prediction for $\sigma_{t\bar{t}} = 6.5$ pb (filled histogram), the background prediction (line histogram), and the signal + background distribution (dashed histogram) [9,14].

The cross section was calculated from the number of $t\bar{t}$ and background candidates above a cut value of the *NN* discriminant. The cut value was chosen to maximize the expected statistical significance $s/\sqrt{s+b}$, where s and b were the number of expected signal and background events. The signal and background distributions were estimated using the TRF prediction and $t\bar{t}$ Monte Carlo events [15]. For both analyses, the expected statistical significance was about 2 standard deviations. The optimal cut for the single (double)-tag analysis was $NN \geq 0.81(0.78)$ shown by a vertical line in Figs. 9 and 10. Table II gives the observed numbers of events (N_{obs}^i), the background prediction (N_{bg}^i), and the efficiency for signal ($\varepsilon_{t\bar{t}}^i$) that can be used to calculate the $t\bar{t}$ production cross section via

$$\sigma_{t\bar{t}} = \frac{N_{obs}^i - N_{bg}^i}{\varepsilon_{t\bar{t}}^i \mathcal{L}(1 - \varepsilon_{TRF}^i)}, \tag{2}$$

where i was "$= 1$" for the single-tag analysis and "≥ 2" for the double-tag analysis. The number of background events is predicted using the TRF method. It was likely that at values of *NN* close to unity a certain fraction of the sample used to predict the background actually consists of
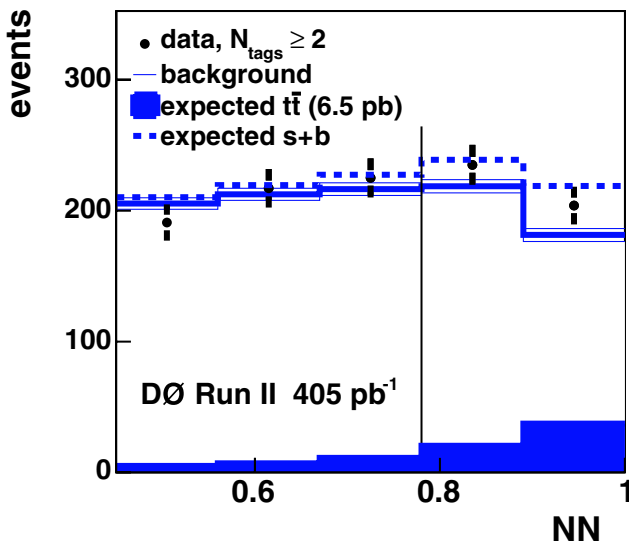
TABLE II. Overview of observed events, background predictions, and efficiencies.

	Symbol	Value
Observed events	$N_{obs}^{=1}$	495
Background events	$N_{bg}^{=1}$	464.3 ± 4.6(syst)
$t\bar{t}$ efficiency	$\varepsilon_{t\bar{t}}^{=1}$	$0.0242_{-0.0058}^{+0.0049}$(syst)
$t\bar{t}$ contamination	$\varepsilon_{TRF}^{=1}$	0.245 ± 0.031(syst)
Observed events	$N_{obs}^{\geq 2}$	439
Background events	$N_{bg}^{\geq 2}$	$400.2_{-6.2}^{+7.3}$(syst)
$t\bar{t}$ efficiency	$\varepsilon_{t\bar{t}}^{\geq 2}$	$0.0254_{-0.0070}^{+0.0065}$(syst)
$t\bar{t}$ contamination	$\varepsilon_{TRF}^{\geq 2}$	0.194 ± 0.048(syst)

tagged or untagged $t\bar{t}$ events, resulting in an increased background prediction. The expected $t\bar{t}$ contamination of the background sample was corrected by a factor ε_{TRF}^i. In the higher value bins of *NN*, the contribution from untagged $t\bar{t}$ events was significant. ε_{TRF}^i was estimated by applying the TRF on $t\bar{t}$ MC and comparing the predicted tagging probability for signal to what was expected from background. The size of the Monte Carlo sample dominates the uncertainty on ε_{TRF}^i.

Table II lists the systematic uncertainties on the estimate of the number of background events, the selection efficiency and the background contamination. The first was uncorrelated between the two analyses, while the latter two were correlated as they were derived from the same Monte Carlo samples.

For the single-tag analysis, the systematic uncertainty on the selection efficiency was dominated by the uncertainty in the jet calibration and identification, which were estimated by varying the parameterizations used by 1 standard deviation. The uncertainty on the background prediction was dominated by the uncertainty on the TRF method and the uncertainty on ε_{TRF} was due to limited Monte Carlo statistics. The uncertainty of the TRF prediction was comprised from the uncertainties coming from the fits of the probability density functions at the jet level, the statistics of the background sample, and the uncertainty on the normalization and correlation factors SF and C_{ij}. For the double-tag analysis, the contribution from the uncertainties due to calibration of the b quark jet identification efficiency was an additional systematic uncertainty on $\varepsilon_{t\bar{t}}$. These uncertainties were derived by varying the parameterizations used within their known uncertainties.

The single-tag analysis yielded a cross section of

$$\sigma_{t\bar{t}} = 4.1_{-3.0}^{+3.0}(\text{stat})_{-0.9}^{+1.3}(\text{syst}) \pm 0.3(\text{lumi}) \text{ pb}. \tag{3}$$

For the double-tag analysis the measured cross section was

$$\sigma_{t\bar{t}} = 4.7_{-2.5}^{+2.6}(\text{stat})_{-1.4}^{+1.7}(\text{syst}) \pm 0.3(\text{lumi}) \text{ pb}. \tag{4}$$

As the single-tag and double-tag analysis were measured on independent samples, the statistical uncertainties were

FIG. 10 (color online). The distribution of the *NN* output variable for double-tag events. Shown are the data (points), background (hashed band), signal (filled histogram), and signal + background (dashed histogram). The vertical line represents the used cut of $NN > 0.78$.

uncorrelated. The uncertainties on the selection efficiency were completely correlated. Taking all uncertainties into account, a combined cross section measurement of

$$\sigma_{t\bar{t}} = 4.5^{+2.0}_{-1.9}(\text{stat})^{+1.4}_{-1.1}(\text{syst}) \pm 0.3(\text{lumi}) \text{ pb} \qquad (5)$$

was obtained, for a top quark mass of $m_t = 175 \text{ GeV}/c^2$. For a top quark mass of $m_t = 165 \text{ GeV}/c^2$, the cross section is $\sigma_{t\bar{t}}(165) = 6.2^{+2.8}_{-2.7}(\text{stat})^{+2.0}_{-1.5} \times (\text{syst}) \pm 0.4(\text{lumi})$ pb, while for a top quark mass of $m_t = 185 \text{ GeV}/c^2$ the value shifted down to $\sigma_{t\bar{t}}(185) = 4.3^{+1.9}_{-1.8}(\text{stat})^{+1.4}_{-1.0}(\text{syst}) \pm 0.3(\text{lumi})$ pb.

In summary, we have measured the $t\bar{t}$ production cross section in $p\bar{p}$ collisions at $\sqrt{s} = 1.96$ TeV in the fully hadronic decay channel. We used lifetime b-tagging and an artificial neural network to distinguish $t\bar{t}$ from back-ground. Our measurement yields a value consistent with SM predictions and previous measurements.

[1] V. M. Abazov *et al.* (D0 Collaboration), Nucl. Instrum. Methods Phys. Res., Sect. A **565**, 463 (2006).

[2] T. Andeen *et al.*, FERMILAB Report No. TM-2365-E, 2006.

[3] The efficiency for signal remained between 85% and 90% throughout the data collection period. Efficiencies were estimated on $t\bar{t}$ Monte Carlo both using a simulation of the trigger system and using parameterizations derived from data.

[4] M. L. Mangano *et al.*, J. High Energy Phys. 07 (2003) 001.

[5] T. Sjöstrand *et al.*, Comput. Phys. Commun. **135**, 238 (2001).

[6] D. Lange, Nucl. Instrum. Methods Phys. Res., Sect. A **462**, 152 (2001).

[7] G. C. Blazey *et al.*, in *Proceedings of the Workshop: QCD and Weak Boson Physics in Run II*, edited by U. Baur, R. K. Ellis, and D. Zeppenfeld (Fermilab, Batavia, IL, 2000).

[8] V. M. Abazov *et al.* (D0 Collaboration), Phys. Lett. B **626**, 35 (2005).

[9] V. M. Abazov *et al.* (D0 Collaboration), Phys. Rev. D **74**, 112004 (2006).

[10] W.-M. Yao *et al.*, J. Phys. G **33**, 1 (2006).

[11] B. Abbott *et al.* (D0 Collaboration), Phys. Rev. Lett. **83**, 1908 (1999).

[12] The possibility that the wrong permutations of jets could be chosen was taken into account in the determination of the values of 79, 11, and 21 GeV/c^2 for M_W, σ_{M_W}, and σ_{m_t}.

[13] R. Brun and F. Rademakers, Nucl. Instrum. Methods Phys. Res., Sect. A **389**, 81 (1997). See also http://root.cern.ch/.

[14] N. Kidonakis and R. Vogt, Phys. Rev. D **68**, 114014 (2003).

[15] The expected $t\bar{t}$ content used to optimize the *NN* cut was estimated using a hypothetical cross section of $\sigma_{t\bar{t}} = 6.5$ pb. The chosen cuts are stable under variation of the $t\bar{t}$ cross section assumed during the optimization.